AN EXPLANATION FOR THE "SWITCH-ON" NATURE OF MAGNETIC ENERGY RELEASE AND ITS APPLICATION TO CORONAL HEATING

R. B. Dahlburg

Laboratory for Computational Physics and Fluid Dynamics, Naval Research Laboratory, Washington, DC 20375-5344

J. A. Klimchuk and S. K. Antiochos

Space Science Division, Naval Research Laboratory, Washington, DC 20375

rdahlbur@lcp.nrl.navy.mil

ABSTRACT

A large class of coronal heating theories postulate that the random mixing of magnetic footpoints by photospheric motions leads to the formation of current sheets in the corona and, consequently, to energy release there via magnetic reconnection. Parker pointed out that, in order for this process to supply the observed energy flux into the corona, the stress in the coronal magnetic field must have a fairly specific value at the time that the energy is released. In particular, he argued that the misalignment between reconnecting flux tubes must be roughly 30° in order to match the observed heating. No physical origin for this number was given, however. In this paper, we propose that secondary instability is the mechanism that "switches-on" the energy release when the misalignment angle in the corona reaches the correct value. We calculate both the 3D linear and fully nonlinear development of the instability in current sheets corresponding to various misalignment angles. We find that no secondary instability occurs for angles less than about 45°, but for larger angles the instability grows at a rapid rate, and there is an explosive release of energy. We compare our results with the observed properties of the corona, and discuss the implications for future observations.

Subject headings: magnetohydrodynamics—Sun: coronal heating—Sun: magnetic fields

1. INTRODUCTION

There is widespread agreement that many coronal phenomena involve the release of free energy that is stored within stressed, current-carrying magnetic field configurations. Highly explosive events such as flares and coronal mass ejections are almost certainly explained in this way (Klimchuk 2001; Forbes 2002), and there is good reason to believe that less dramatic phenomena, such as the heating of coronal loops, also involve the conversion of magnetic energy (e.g., Mandrini, Démoulin, & Klimchuk 2000). While an ample supply of magnetic free energy is clearly present in the corona, the process by which it is converted into heat and other forms remains a nagging unsolved problem. Any viable explanation must satisfy three conditions. The energy release mechanism must: 1, remain dormant long enough for the magnetic stresses to build to the required levels; 2, proceed rapidly (at least as fast as the buildup rate) once it begins; and 3, convert enough of the available free energy to explain a particular phenomenon.

Energy release mechanisms that satisfy the second and third conditions have been known for some time, including Petschek-type magnetic reconnection, but they have not been demonstrated to have the "switch-on" property required by observations. In this paper, we consider a promising mechanism called the secondary instability, which appears to satisfy all three conditions. This instability has been known for some time, but its tendency to activate only after magnetic stresses exceed a threshhold has heretofore not been appreciated. As discussed in detail in earlier works (Dahlburg, Antiochos, & Zang 1992; Dahlburg 1997; Schumacher & Seehafer 2000; Dahlburg & Einaudi 2002), the energy release occurs at current sheets and proceeds in four stages: 1, the current sheet equilibrium is destabilized by a two-dimensional (2D) resistive instability (the primary instability); 2, the resistive disturbance grows until it saturates nonlinearly to form a 2D secondary equilibrium; 3, the 2D equilibrium is itself destabilized by a three-dimensional (3D) ideal instability (the secondary instability); and 4, the 3D disturbance grows to large amplitude and transitions to turbulence with enhanced energy dissipation. In this paper, we show that the secondary instability occurs only in current sheets across which the magnetic field rotates by a sufficiently large angle. Thus, if the angle increases with time, as is the case when magnetic configurations are subjected to time-dependent shearing, the instability would switch on only after the critical angle is reached.

The importance of the "switch-on" nature of the energy release cannot be overstated. To illustrate this point, consider the well-known picture of coronal heating advocated by Parker (1983a,b; 1988) and recently revisited by Priest, Heyvaerts, & Title (2002). Parker proposed that random displacements of magnetic footpoints in the photosphere cause the coronal field to become wrapped and braided in complicated ways, perhaps resembling a

bowl of tangled spaghetti. He further suggested that magnetic energy is released explosively as nanoflares at the interfaces between adjacent misaligned flux tubes. From global energy balance considerations, Parker estimated how large the angle of misalignment must become before a nanoflare occurs. Footpoint stressing motions pump energy into the coronal field at a rate given by the Poynting flux through the solar surface:

$$F = \frac{1}{4\pi} B_y B_x v_x, \tag{1}$$

where B_y is the vertical component of the field and B_x is the horizontal component in the direction of motion, which has velocity v_x. By equating this flux with the combined radiation losses from the corona and transition region (which is heated by downward thermal conduction from the corona) and by adopting typical observed values for B_y and v_x, Parker concluded that $B_x \approx 0.25 B_y$ for a nanoflare to occur. This corresponds to a shear angle between adjacent flux tubes of $\theta = 2 \arctan(0.25) \approx 30^\circ$. For smaller angles, the Poynting flux would be inadequate to power the observed radiation losses, while for larger angles, the implied radiation would be too great.

We show here that the secondary instability has an angular dependence consistent with observations. Our approach involves a series of numerical MHD simulations of perturbed semi-infinite current sheet configurations. Each configuration has a fixed shear, or magnetic field rotation, but the shear varies from one configuration to the next. We find that weakly sheared configurations are stable, while strongly sheared configurations are unstable. Our preliminary results were presented in Dahlburg, Klimchuk, & Antiochos (2003). The details of the numerical model are described in Section 2, and the results of linear and nonlinear simulations are presented in Sections 3 and 4, respectively. The physical interpretation of the instability is discussed in greater detail in Section 5. Section 6 is concerned with the thickness of coronal current sheets and is necessary for the discussion of coronal heating in Section 7. The paper ends with a summary and final conclusions, as well as some discussion about future directions of this research.

2. NUMERICAL MODEL

We adopt the current sheet geometry that is shown schematically in Figure 1. The undisturbed background magnetic field has normalized shear ($\mathbf{B}_{0x}$) and guide ($\mathbf{B}_{0y}$) components given by

$$\mathbf{B}_{0x}(z) = C \tanh(z) \hat{\mathbf{e}}_x, \qquad \mathbf{B}_{0y} = 1 \hat{\mathbf{e}}_y, \tag{2}$$

where z is in units of the sheet halfwidth (l). The field rotates across the sheet by a total angle $\theta = 2 \arctan(C)$. Thus, $C = \tan(\theta/2) = B_{0x}(z = \infty)/B_{0y}$ is a parameter that measures

the shear. The initial velocity is taken to be zero. Note that the field is not force free and so there is a mechanical pressure gradient given by the condition $dp/dz = \nabla \times \mathbf{B_0} \times \mathbf{B_0}$. This simplified 1D field, with quantities varying only in the z-direction, is meant to represent a subregion within a much larger 3D configuration (e.g., a "patch" at the interface between two misaligned coronal flux tubes). Readers should not misconstrue θ as the pitch angle of the magnetic field within a twisted flux tube.

We solve numerically the dissipative, incompressible, magnetohydrodynamic (MHD) equations, written in a dimensionless rotation form:

$$\frac{\partial \mathbf{v}}{\partial t} = \mathbf{v} \times \boldsymbol{\zeta} - \nabla \Pi + \mathbf{j} \times \mathbf{B} + \frac{1}{S_v} \nabla^2 \mathbf{v}, \tag{3a}$$

$$\nabla \cdot \mathbf{v} = 0, \tag{3b}$$

$$\frac{\partial \mathbf{B}}{\partial t} = \nabla \times \mathbf{v} \times \mathbf{B} - \frac{1}{S} \nabla \times \mathbf{j}, \tag{3c}$$

and

$$\nabla \cdot \mathbf{B} = 0, \tag{3d}$$

where $\mathbf{v}(\mathbf{x}, t) \equiv$ flow velocity, $\boldsymbol{\zeta}(\mathbf{x}, t) = \nabla \times \mathbf{v} \equiv$ vorticity, $\mathbf{B}(\mathbf{x}, t) \equiv$ magnetic field, $\mathbf{j}(\mathbf{x}, t) =$

$\nabla \times \mathbf{B} \equiv$ electric current density, $\Pi(\mathbf{x}, t) \equiv$ mechanical pressure + kinetic energy density, $S \equiv$ Lundquist number, and $S_v \equiv$ viscous Lundquist number. The resisivity and viscosity are assumed to be constant and uniform. We measure distance in units of the current sheet halfwidth (l), magnetic field in units of the guide field (B_{0y}), velocity in units of the Alfvén speed (V_A), and time in units of the Alfvén transit time across the sheet ($\tau_A = l/V_A$). The simulations are carried out with our 3D Fourier pseudospectral–Fourier collocation code (Dahlburg *et al.* 1992) in which the magnetic and velocity fields are expanded in the form:

$$\mathbf{B}(x, y, z, t) = \sum_{|m| \le M/2} \sum_{|n| \le N/2} \sum_{p=0}^{P} \tilde{\mathbf{B}}(m, n, p, t) \; e^{i(m\alpha x + n\beta y)} \; f_i(Z), \tag{4a}$$

$$\mathbf{v}(x, y, z, t) = \sum_{|m| \le M/2} \sum_{|n| \le N/2} \sum_{p=0}^{P} \tilde{\mathbf{v}}(m, n, p, t) \; e^{i(m\alpha x + n\beta y)} \; f_i(Z), \tag{4b}$$

where

$$f_i(Z) = \begin{cases} \cos(pZ) & i = x, y; \\ \sin(pZ) & i = z \end{cases} \tag{4c}$$

and i denotes the three Cartesian directions. The spatial variable Z is a transformation of z such that $-\infty \le z \le \infty$ maps onto $-1 \le Z \le 1$. The smallest wavenumbers (longest wavelengths) treated in our system are α in the x direction and β in the y direction. Thus, the

simulation box has effective dimensions: $0 \leq x \leq 2\pi/\alpha$; $0 \leq y \leq 2\pi/\beta$; and $-L_z \leq z \leq L_z$. Periodic boundary conditions are imposed in the x and y directions and free-slip boundary conditions in the z direction.

As described above, the energy release we are studying involves four distinct stages, beginning with the linear growth of the primary instability and ending with a nonlinear transition to turbulence of the secondary instability. Treating all four stages with a single do-it-all simulation is not numerically feasible. We therefore begin each simulation near the end of the first stage, when the primary instability is close to saturation. We approximate this state by modifying the initial equilibrium of Equation 2 with a large amplitude dose of its fastest growing unstable eigenmode. Earlier studies have shown this to be a long wavelength 2D mode with wavenumber $k_x \approx 0.2$ (Dahlburg et al. 1992; Dahlburg & Karpen 1995; Seehafer & Schumacher 1998). Essentially it consists of a series of straight infinite flux tubes lined up side-by-side along the current sheet and directed parallel to the y-axis. When viewed in cross section, the tubes produce the familiar chain of resistive tearing islands. By choosing $\alpha = 0.2$, we associate this most unstable eigenmode with the $(m, n) = (1, 0)$ mode in our expansion in Equation 4. The spatial dependence $f_i(Z)$ is simply the eigenfunction obtained by solving the linearized eigenvalue problem using a Chebyshev-τ technique (Dahlburg et al. 1992).

To initiate the secondary instability, which has important structure in the y direction, we further modify the equilibrium with a small amplitude dose of its $(m, n) = (1, 1)$ eigenmode. Although 3D modes (defined as modes with $n \neq 0$) grow slowly in the original equilibrium, they grow rapidly in the new equilibrium that is formed when the primary instability saturates. The initial magnetic and velocity fields of our simulations are thus given by:

$$\mathbf{B}(x, y, z, t = 0) = \mathbf{B}_0(z) + \epsilon_{2D}\mathbf{B}_{2D}(z)e^{i\alpha x} + \epsilon_{3D}\mathbf{B}_{3D}(z)e^{i(\alpha x+\phi)+i\beta y} \tag{5a}$$

and

$$\mathbf{v}(x, y, z, t = 0) = \epsilon_{2D}\mathbf{v}_{2D}(z)e^{i\alpha x} + \epsilon_{3D}\mathbf{v}_{3D}(z)e^{i(\alpha x+\phi)+i\beta y}, \tag{5b}$$

where $\mathbf{B}_0(z)$ is the unperturbed background field, $\mathbf{B}_{2D}$ and $\mathbf{v}_{2D}$ are from the $(1, 0)$ eigenmode, and $\mathbf{B}_{3D}$ and $\mathbf{v}_{3D}$ are from the $(1, 1)$ eigenmode. We impose a phase shift $\phi = \pi/2$ between the eigenmodes. The primary instability is known to saturate at an amplitude of approximately 0.01 (see Dahlburg 1998), and we therefore choose a somewhat smaller initial amplitude of $\epsilon_{2D} = 0.002$ or 0.003, depending on the run. This amplitude refers to the x component of the perturbed magnetic field, normalized to the background, B_{0y}. The y and z components and all components of the perturbed velocity are scaled accordingly. We use different initial amplitudes for the 3D eigenmode. For the linear simulations, we begin with an extremely small perturbation $\epsilon_{3D} = 10^{-14}$, and for the nonlinear simulations, we begin

with a larger but still small $\epsilon_{3D} = 5 \times 10^{-6}$ or 10^{-3}, again depending on the run. Table 1 indicates the parameter values used for the simulations shown in the figures. In all cases, $\alpha = 0.2$ and $L_z = 250$; $\beta = 0.2$ except in Figures 3 and 4.

3. LINEAR GROWTH OF THE SECONDARY INSTABILITY

To follow the linear development of the secondary instability, it is sufficient to truncate our expansion in Equation 4 at $N = 2, M = 16$, and $P = 16$. We consider a series of runs in which C varies between 0.1 and 1.0. As a measure of the growth of the instability, we compute the energies in the different modes by integrating over the computational box:

$$E_{mn}(t) = \frac{\pi^2}{2\alpha\beta} \int_{-L_z}^{L_z} [|\mathbf{B}_{mn}(z,t)|^2 + |\mathbf{v}_{mn}(z,t)|^2] dz \tag{6}$$

where

$$\mathbf{B}_{mn}(z,t) = \sum_{p=0}^{P} \quad \tilde{\mathbf{B}}(m,n,p,t) \quad f_i(Z) \tag{7a}$$

and

$$\mathbf{v}_{mn}(z,t) = \sum_{p=0}^{P} \quad \tilde{\mathbf{v}}(m,n,p,t) \quad f_i(Z). \tag{7b}$$

The energy of the secondary instability is then determined by summing over the 3D modes with $n = 1$:

$$E_{3D}(t) = \sum_{m} E_{m\ 1}(t). \tag{8}$$

Higher order 3D modes are not significant in the linear regime. The evolution of E_{3D} is illustrated in Figure 2. We see that the energy grows with time only for $C > 0.4$. Thus, for these model parameters, the secondary instability is linearly unstable only when the shear angle exceeds $\theta \approx 2 \arctan(0.4) = 44°$. The growth times in Figure 2 range from $68\tau_A$ for $C = 0.5$ down to $6.6\tau_A$ for $C = 1.0$. Since $\tau_A \sim 0.1$ s (see below), the instability is very fast. The deviation from a pure exponential (straight line) for the unstable C and the slow energy decay for the stable C are due to Ohmic and viscous dissipation.

Our choice $\beta = 0.2$ is somewhat arbitrary, so to determine whether the choice is important, we consider a second set of simulations using $\beta = 0.1$. The evolution of E_{3D} is shown in Figure 3. The behavior is qualitatively very similar to the $\beta = 0.2$ case, although there are some minor differences. The growth times are slightly longer, but as before, instability first occurs when C exceeds 0.4.

To further investigate the dependence on β, we performed a several runs at $C = 1.0$ with different values of β and several values of the Lundquist numbers. Growth rates of E_{3D} are plotted as a function of β in Figure 4. They peak near $\beta = 0.5$, but are not appreciably different at 0.2, the value used for most of our runs. We also see that the growth rate increases with Lundquist number for our runs. We believe this is due, in part, to the fact that the basic x-magnetic field (initially equal to $\tanh z$) decays at a rate dependent on S during the time in which the primary instability grows and eventually attains finite amplitude. Thus, when the secondary instability begins to grow the basic magnetic field is different for the different values of S and S_V. Also, the secondary instability may itself be weakly dependent on the resistivity.

4. NONLINEAR EVOLUTION OF THE SECONDARY INSTABILITY

To investigate whether the secondary instability grows to sufficient amplitude to be energetically important requires a nonlinear treatment. This necessitates the inclusion of many more modes in the expansion in Equation 4. We use $N = M = P = 128$. Because of the extra computational demands that this imposes, we start each simulation with a much larger 3D perturbation of $\epsilon_{3D} = 5 \times 10^{-6}$.

Figure 5 shows the evolution of several individual modes for cases of weak ($C = 0.1$) and strong ($C = 1.0$) shear. Plotted are the volume integrals of the magnetic energies of each of the modes. Recall that we initialize each simulation with a modest dose of the $(1, 0)$ eigenmode, to place the system close to the nonlinear saturation of the primary 2D resistive instability, as well as a small dose of the $(1, 1)$ eigenmode, to initiate three-dimensional evolution. These modes therefore have finite amplitude at $t = 0$ in the figures. Let us first consider the case of weak shear (Figure 5a). The initial 2D perturbation grows until saturation at about $t = 250$. As it does, it excites higher order 2D modes, which are also resistively unstable and saturate at roughly the same time. Thereafter, all the modes decay slowly due to Ohmic and viscous dissipation. The imposed 3D perturbation decays from the very start, as expected from our linear results.

The 2D modes evolve very similarly in the case of strong shear (Figure 5b). They saturate at a higher level because there is 100 times more energy in the shear component of the background field ($C^2 = 1.0$ versus 0.01). The 3D modes exhibit a dramatically different behavior, on the other hand. They decay initially due to Ohmic and viscous effects, but then they undergo rapid growth as the primary instability saturates and the secondary instability takes off. This is striking evidence of how the primary instability creates the conditions that are necessary for the secondary instability to occur. The 3D modes finally saturate at about

$t = 1000$ after increasing by many orders of magnitude.

Figure 6a shows the evolution of the kinetic energies (not magnetic, as in Figure 5) of the individual modes for the strong shear case. In the late stages, all of the 2D modes have considerably smaller energy than the 3D modes. This indicates a cascade of energy toward larger wavenumbers (shorter wavelengths), suggestive of turbulence. The cascade is more clearly evident in Figure 6b, which shows the average kinetic energy wavenumber as a function of time for both the weak and strong shear cases. We obtain this wavenumber simply by computing the square root of the ratio of the enstrophy to the kinetic energy (*cf.* Horiuchi and Sato 1986). For the weak shear case not much change is observed implying the absence of spectral transfer. For the strong shear case, however, a significant increase in this variable is seen as the system becomes nonlinear. The increase in magnitude implies the existence of a direct cascade of energy.

Several important features relating to the development of the secondary instability are portrayed in Figure 7, which shows isosurfaces of the electric current magnitude ($j = |\nabla \times \mathbf{B}|$) well into the nonlinear regime. Note that the orientation is rotated by 90° compared to Figure 1. Figure 7a shows the basically 2D filamentation of the current which occurs as the primary resistive instability saturates to form a secondary equilibrium. The secondary instability initially appears at this time as a slight bending and twisting of the filament but by the time of Figure 7b it has completely overwhelmed the 2D state, and the current structure assumes a purely 3D form. It resembles what might be called a "twisted double fishtail." (Recall that the system is periodic in x and y, so the two "fishtails" are actually connected.) This configuration differs significantly from the serpentine shape seen in simulations with no guide field (Dahlburg, Antiochos and Zang 1992; Dahlburg and Einaudi 2002). The fishtail structure is disrupted by the time of Figure 7c, and the currents assume an arguably turbulent appearance. At late times the system settles down to the state shown in Figure 7d.

The concentration of the electric current on small scales causes an intensification of the current density and an associated increase in Ohmic dissipation. In addition, there is enhanced viscous dissipation due to the complicated flow patterns that develop with regions of large vorticity. Both effects lead to plasma heating. The total heating rate integrated over the computational box is given by:

$$Q = \frac{J}{S} + \frac{\Omega}{S_v} \tag{9}$$

where S is the Lundquist number, S_v is the viscous Lundquist number, Ω is the integrated square of the vorticity (enstrophy),

$$\Omega = \int_{-L_z}^{L_z} \int_0^{2\pi/\beta} \int_0^{2\pi/\alpha} |\nabla \times \mathbf{v}|^2 \, dx \, dy \, dz, \tag{10a}$$

and J is the integrated square of the electric current density,

$$J = \int_{-L_z}^{L_z} \int_0^{2\pi/\beta} \int_0^{2\pi/\alpha} |\nabla \times \mathbf{B}_p|^2 \; dx \; dy \; dz. \tag{10b}$$

Here, $\mathbf{B}_p$ is the perturbed magnetic field defined as:

$$\mathbf{B}_p = (b_x, b_y, b_z), \tag{11}$$

with

$$b_i(x, y, z, t) = B_i(x, y, z, t) - \overline{B}_i(z, t) \tag{12}$$

and

$$\overline{B}_i(z, t) = \frac{\alpha\beta}{4\pi^2} \int_0^{2\pi/\beta} \int_0^{2\pi/\alpha} B_i \; dx \; dy \tag{13}$$

where B_i denotes either B_x, B_y or B_z. We use the perturbed magnetic field rather than the total magnetic field because of the artificially large electrical resistivity and corresondingly small magnetic Lundquist number in our simulations. In the real corona, direct Ohmic dissipation of the equilibrium current sheet is negligible. Significant plasma heating occurs only when the instability produces steep gradients in the magnetic and velocity fields. In contrast, our numerical model has non-negligible dissipation of the current sheet even in the absence of the instability. By using the perturbed magnetic field to compute the current in Equation 10b, we attempt to isolate the heating that is due to the instability alone. Note that all numerical simulations face the problem of unrealistically small Lundquist numbers. Finite numerical resolution produces a small effective Lundquist number even when the explicit number used in the MHD equations is large.

Figure 8 shows the Ohmic and viscous heating rates as a function of time for the strong shear case $C = 1.0$. The profiles are sharply peaked with a full width at half maximum (FWHM) of approximately 200 τ_A. We determine the total energy dissipated by integrating over the duration of the event, t_f:

$$E_d = \int_0^{t_f} Q \; dt. \tag{14}$$

Table 2 gives the results for simulations with shear parameters ranging from $C = 0.1$ to 1.5, using $t_f = 2223$. The energy increases monotonically with shear, but jumps most significantly between $C = 0.7$ and 0.8, i.e., at a shear angle of about 70°.

Since the magnitude of the guide field, B_{0y}, is the same in all simulations, the configurations with larger shear have greater magnetic energy. In particular, the free energy available for plasma heating depends on B_{0x}^2 and therefore scales as C^2. To better evaluate the dependence of heating on shear, we have normalized E_d by C^2 in the third column of Table

2. These values are also plotted as a function of C in Figure 9. We see that the normalized energy remains fairly constant up to $C = 0.7$. This heating is due mostly to the primary instability and is likely to be exaggerated in our simulations due to the small Lundquist numbers. The dramatic increase in normalized energy for $C > 0.7$ is clearly associated with the secondary instability. We note that this is somewhat larger than threshhold for linear instability ($C > 0.4$).

5. INTERPRETATION

We can interpret the secondary instability as a nearly ideal kinking of the twisted flux tubes that form from the primary instability. When C is small, the tubes have minimal twist because the ratio of shear-to-guide field (B_{0x}/B_{0y}) is small in the the initial equilibrium. The ratio increases with increasing C, and so too does the twist of the tubes. Since the kink instability occurs only when a critical twist is exceeded (e.g. Linton, Longcope and Fisher 1996, Linton et al. 1998), we have a natural explanation for why the secondary instability has a threshhold in C.

The well-known condition for flux tube kinking is that the helical field lines execute one complete turn over the wavelength of the unstable mode. From geometrical considerations, we can express this condition as

$$2\pi r \frac{B_y}{B_x} \approx \lambda_y = \frac{2\pi}{k_y}, \tag{15}$$

where r is the characteristic radius of the tube. Flux tubes formed from the primary instability are not perfectly cylindrical, but rather are flattened such that the cross section is wider along the current sheet than across it. From Dahlburg et al. (1992, Fig. 4), we take the characteristic radius to be

$$r \approx \frac{\lambda_x}{4} = \frac{\pi}{2k_x}. \tag{16}$$

Combining Equations 15 and 16, noting that $k_x = k_y$ ($\alpha = \beta$), and taking $B_x/B_y = B_{0x}/B_{0y} = C$, we have

$$C_{crit} \approx \frac{\pi}{2} \tag{17}$$

for the critical shear. Although this is roughly twice as large as the value we found from our nonlinear simulations, the agreement is quite good given given the gross assumptions that were made in deriving the result.

We can gain additional information about the secondary instability by performing a classical energy analysis (Bernstein *et al.*, 1958). Where we calculate the sign of the potential

energy δW of the system:

$$\frac{1}{4\pi}\int\{|\nabla\times(\mathbf{v}_{3D}\times\mathbf{B}_0)|^2-(\mathbf{v}_{3D}\times\nabla\times\mathbf{B}_0)\cdot[\nabla\times(\mathbf{v}_{3D}\times\mathbf{B}_0)]\}d^3x. \tag{15}$$

Here we have replaced the displacement with the velocity, which should not affect the sign of δW. Note that the surface terms drop out due to our boundary conditions. If δW is less than zero, the system is unstable. Figure 10 illustrates, for this run, the steps in the secondary instability process outlined in the Introduction. The 3D mode grows at the primary instability rate [($\omega_i \sim 0.015$ (see Figure 5)] before the 2D mode saturates at about $t \sim 50$. After saturation of the 2D mode, however, the secondary instability is triggered and this 3D mode grows at a much faster rate, ~ 0.09. Although we have not investigated this aspect, we expect that the gap between the 3D primary and secondary growth rates broadens with increasing Reynolds number because the primary mode becomes increasingly damped while the secondary mode growth rate remains nearly constant, as seen already in analyses of the simpler component systems (*e.g.,* Metcalfe *et al.,* 1987, Dahlburg, Antiochos, and Zang, 1992). Note also that our computations indicate that our chosen initial disturbance gives an initial positive value of δW. However, shortly after growth is observed in the 3D energy, δW changes sign and becomes negative, indicative of an ideal instability.

To determine the efficiency and energetics of the secondary instability, we break down the time derivative of total energy into the energy transfer rates among all possible three-dimensional modes plus dissipative losses:

$$\frac{dE_3}{dt}=\tau_{13}+\tau_{23}+\delta_3, \tag{16}$$

where $E_3 = 1/2\langle|\mathbf{B}^{[3]}|^2+|\mathbf{v}^{[3]}|^2\rangle$ represents the magnetic and kinetic energy in the 3D fields, τ_{13} represents the exchange of energy between 1D and 3D fields, τ_{23} represents the exchange of energy between the 2D and 3D fields, and δ_3 represents the resistive and viscous diffusion of the 3D fields. These terms are evaluated fully in Dahlburg (1997).

Hence the normalized rate for energy transfer to and from the 3D mode is

$$\Gamma\equiv\frac{1}{2E_3}\frac{dE_3}{dt}=\frac{\tau_{13}}{2E_3}+\frac{\tau_{23}}{2E_3}+\frac{\delta_3}{2E_3}=T_{13}+T_{23}+D_3. \tag{17}$$

In previous work on a related problem in which the sheared magnetic field was held fixed while the guide magnetic field magnitude was varied (Dahlburg 1995), we have shown that changing the relative magnitude of the fieldwise and sheetwise magnetic field components has a large effect on T_{13}, and a much smaller effect on T_{23} and D_3. That is also the case here. In Figure 11 we show T_{13} as a function of time for cases with $C = 0.3$ and $C = 0.4$ for the

same situation as shown in Figure 2. These values of the shear parameter (C) bracket the instability threshold, *i.e.,* for $C = 0.3$ the secondary instability does not occur, whereas for $C = 0.4$ the secondary instability does occur. For both values of C there is an initial phase during which T_{13} is noisy, indicating that the 3D instability has not yet emerged. Later for $C = 0.3$ we see that T_{13} wanders around zero, whereas for $C = 0.4$ the term T_{13} remains positive, indicating a net transfer of energy from the 1D to the 3D fields. Hence it appears that the T_{13} term is crucial in secondary instability energy transfer.

6. CURRENT SHEETS

In order to apply our results to the Sun, we must convert the dimensionless variables of our simulations into the corresponding physical quantities. Most of the normalization factors involved in this conversion, including the coronal magnetic field strength and coronal Alfvén speed, are well known from observations, but the thickness of current sheet is not. We here estimate a thickness based on the coronal heating picture of Parker (1994) and Priest et al. (2002). Our estimate may not apply to other situations, such as flares and coronal mass ejections, where the current sheet thickness could be much different.

Although our understanding of the photospheric magnetic field is still evolving, there is a general concensus that much of the flux is contained within small concentrations of intense field, often referred to as kiloGauss (kG) flux tubes (e.g., Solanki 1993; Muller 1994). These concentrations may not be as tube-like as once thought (Berger & Title 1996), but such a description is a reasonable approximation for our purposes here. The flux tubes flare out dramatically in the chromosphere and transition region, and if there were no surrounding flux, they would come into contact with their neighbors at very low heights in the corona. Any relative motion of the footpoints, as produced by photospheric convection for example, would then generate extremely thin current sheets at the coronal interfaces. In reality, appreciable flux does exist between the kG tubes (e.g., Meunier, Solanki, & Livingston 1998; Stenflo, Keller, & Gandorfer 1998; Lin & Rimmele 1999), and it plays a major role in determining the thickness of the coronal current sheets. We refer to this flux as "weak flux" because its field strength in the photosphere is considerably less than that of the kG tubes. In the corona, where the plasma β is small, the field strengths of the tubes and surrounding flux must be approximately equal in order to have lateral force balance.

To estimate the effect of the weak flux, imagine that the solar surface is partitioned into pieces, each associated with a single kG flux tube that lies at its center. For simplicity, we assume that the pieces and the flux tube cross sections have square shapes, as shown in Figure 12. The drawing on the left shows a layer in the photosphere, and the drawing on

the right shows an overlying layer in the corona, above where the tube has flared out. Let the transverse size of the tube be designated by d_p in the photosphere and d in the corona. From flux conservation,

$$B_p d_p^2 = B d^2, \tag{18}$$

where B_p and B are the magnetic field strengths of the tube in the photosphere and corona, respectively. Because the coronal field strength is approximately the same inside and outside the tube, the fraction of the total flux that is contained in the tube is roughly equal to the tube's fractional area in the corona:

$$f = \frac{d^2}{(d+2w)^2}, \tag{19}$$

where w is the halfwidth of the lane of weak flux that surrounds the tube (one-half the tube separation). Combining Equations 18 and 19 gives

$$w = \frac{1}{2}\left(f^{-\frac{1}{2}} - 1\right)\left(\frac{B_p}{B}\right)^{\frac{1}{2}} d_p. \tag{20}$$

Photospheric observations indicate that $B_p \approx 1500$ G, $d_p \approx 200$ km, and $f \approx 0.5$ (e.g., Solanki 1993; Meunier et al. 1998). It is possible that many flux tubes have a smaller diameter. Taking $B = 30$ G for an average coronal field strength in active regions (Mandrini, Demoulin & Klimchuk, 2000), we have that $w \approx 300$ km or less.

The relationship between w and the current sheet halfwidth, l, depends on a number of factors, but especially the pattern of mass flows in the photosphere. If the flows have a scale comparable to the flux tube separation, then the current sheet will occupy the entire volume between the tubes, and $l \approx w$. If the flows instead have narrow regions of extreme shear, like the faults of an earthquake, the current sheet will be much thinner than w. Another contributing factor is the shape of the flux tube cross section. Our idealized picture of square cross sections maximizes the tube separation. Tubes with circular cross sections, which are more likely if the tubes are twisted (Klimchuk, Antiochos, & Norton, 2000), would have a distance of closest approach that is considerably less than w, as indicated in Figure 13. Small separations are also expected if the tubes are wrapped around eachother, since magnetic tension would act to pull the tubes together and push the intervening weak flux out of the way. All things considered, it seems reasonable to assume that the typical halfwidth of coronal current sheets is less than and perhaps much less than 100 km.

We note in passing that the choice $\alpha = 0.2$ places an upper limit on the ratio l/w. The current sheet dimension in the x-direction must obviously be smaller than the flux tube diameter, d, and therefore the x-dimension of our numerical box must also be smaller than d. In physical units, $L_x = 2\pi l/\alpha \approx 31.4\ l < d$. For $f = 0.5$, Equation 19 gives $d = 4.8w$, and therefore $l/w < 0.15$. This seems reasonable based on the discussion above.

7. IMPLICATIONS FOR CORONAL HEATING

We are now ready to evaluate whether the secondary instability is a viable mechanism for coronal heating. As discussed in the Introduction, there are three basic requirements that must be satisfied: 1, the instability must remain dormant until the magnetic field has become sufficiently stressed; 2, it must proceed rapidly (at least as rapidly as the energy buildup rate) once it switches on; and 3, it must convert a sufficiently large fraction of the stored magnetic energy. We have already shown that the first requirement is satisfied. The secondary instability has a critical shear angle that agrees well with the angle inferred from observations. Both angles are of order a few tens of degrees, which is quite impressive given that either angle could have been within a small fraction of a degree of 0° or 180°.

To address the second requirement, we adopt a typical coronal Alfvén speed $V_A = 1000$ km s^{-1} and current sheet halfwidth $l = 100$ km. The Alfvén transit time is then $\tau_A = 0.1$ s. With these units, we see from Figures 2, 3, and 8 that the secondary instability has a linear growth time of order 1 s and a nonlinear energy dissipation growth time of order 20 s. In comparison, the coronal field is stressed on a timescale given by $L/V_p = 10^5$ s, where $L = 10^5$ km is a typical coronal loop length and $V_p = 1.0$ km s^{-1} is a typical photospheric velocity. The secondary instability therefore easily satisfies the requirement of being rapid. The growth rate of the primary instability is also very important, but we defer discussion of it until later.

Regarding the third requirement, we note from Table 2 and Figure 8 that the total energy dissipated during a heating event has a dimensionless value of roughly 200. To convert to physical energy, we multiply by $B^2 l^3/8\pi$. Taking $B = 30$ G and $l = 100$ km, we obtain $E_d = 7 \times 10^{24}$ ergs. This is a substantial energy release. It exceeds the canonical nanoflare energy of 3×10^{23} ergs first suggested by Parker (1994, pg. 357), although both values are highly approximate.

In order for events of this magnitude to explain the heating of the corona, they must occur with a sufficient spatial density and temporal frequency. From Figure 13, we estimate that there are somewhat less than $2/d^2$ current sheets per unit area across the solar surface, where d is the coronal diameter of a kG flux tube. Each of these current sheets can support roughly L/L_y heating events along its length, where L is a typical coronal loop halflength and $L_y = 2\pi l/\beta$ is the y-dimension of our numerical box. If the events recur with a characteristic time interval $\Delta\ t$ at each location, the flux of energy losses that could be powered by the events is given by

$$F = \frac{\beta}{\pi} \frac{L}{l} \frac{B}{B_p} \frac{E_d}{d_p^2\, \Delta t}, \tag{21}$$

where we have made use of Equation 18. Using previously adopted values for L, l, B, and

B_p, and taking $d_p = 200$ km, we find that observed energy flux from active regions, $F = 10^7$ ergs cm^{-2} s^{-1} (Withbroe & Noyes, 1977), can be explained with an event recurrence interval of $\Delta\, t \approx 2000$ s. This interval seems quite plausible. It is both longer than the typical event duration (100 s) and shorter than the magnetic field stressing time (10^5 s).

How heating events recur at a particular location is something that we plan to explore in depth in a future study. It requires that "processed" magnetic flux from one event move aside so that new flux can "load up" the current sheet for the next event. Such behavior is not possible in the doubly-periodic geometry of our present calculations. However, in the fully 3D geometry of a finite current sheet, processed flux will naturally be expelled from the sheet (in the direction of the vertices in Figure 13) due to the magnetic tension in the reconnected field lines. Whether a series of distinct heating events occurs or whether the instability developes into a quasi-steady Petschek-like reconnection remains to be determined.

We now return to the issue of the primary instability growth rate. As we have emphasized, the secondary instability begins only after the primary instability has modified the current sheet equilibrium. To explain coronal heating, the growth time of the primary instability must be shorter than the stressing time of the magnetic field. Because the primary instability is resistive, its dimensionless growth time increases with the Lundquist number, approximately as $S^{0.9}/4$. For a classical diffusivity of $\eta = 1.0 \times 10^{-6}$ km^2 s^{-1} (Priest, 1982, pg. 79), $S = V_A l/\eta \sim 10^{11}$ and the growth time is an extremely long 2×10^9 s. Thinner current sheets would have shorter growth times, but it is clear that in order for this mechanism to have relevance for the Sun, the diffusivity must be greatly enhanced compared to its classical value.

The secondary instability is not unusual in this regard. Most theories of coronal heating require anomolously large transport coefficients. This includes the popular ideas of steady reconnection (Parker 1972; Biskamp 1993, Sec. 6.2.2; Priest & Forbes 2000, Sec 5.4.) and wave heating by resonance absorption (Ofman, Davila, & Steinolfson 1994). Recent observations provide compelling evidence that transport coefficients are indeed greatly enhanced. Nakariakov et al. (1999) studied transverse loop oscillations observed by *TRACE* and concluded that the rapid damping requires an effective Lundquist number of $S = 10^6$ (although see the concerns raised by Solovév, Mikhalyaev, & Kiritchek, 2002). Using this value, the growth time of the primary instability is only 6×10^4 s, less than the magnetic field stressing time.

8. FINAL REMARKS

Our results suggest that the secondary instability is a very promising explanation of coronal magnetic energy release, expecially in the context of coronal heating. As far as we are aware, it is the only mechanism so far proposed that has the necessary switch on property. This is a fundamental property that, in our view, has been greatly underappreciated. It is required to explain a whole host of coronal phenomena, not only coronal heating.

While we are very encouraged by our initial results, much more work needs to be done before the secondary instability is established as playing a central role in coronal energy release. On the theoretical side, we must relax some of the assumptions that restrict our current simulations. First, we need to examine the consequences of finite current sheet dimensions. Our infinite current sheet geometry prevents us from studying the "reloading" of the current sheet that is required for multiple events, and it eliminates line tying effects that could potentially be important. Second, we need to investigate time-dependent shearing. We have thusfar assumed a background field that is constant in each simulation. This is reasonable once the highly explosive secondary instability begins, but it may not be appropriate for the much slower primary instability. We have emphasized that the primary instability creates a modified equilibrium in which the secondary instability can occur. The properties of this equilibrium will be different if the shear of the background field is changing as the primary instability grows. This is likely to influence the secondary instability. For example, the narrow flux tubes that are created by the resistive tearing of the current sheet will have different twist profiles, $\phi(r)$, with the outer "shells" of the tubes being more highly twisted than the inner cores. It is known that the properties of the kink instability depend on the details of the twist profile (e.g., Lionello et al. 1998). Some profiles produce a global kinking of the tube, while others produce an internal rearrangement of the field, leaving the global structure essentially unchanged. How this may affect the secondary instability is an open question.

We also need to determine whether the response of the coronal plasma to secondary instability heating is consistent with soft X-ray and EUV observations. This effort will likely involve one-dimensional hydrodynamic loop modeling, at least initially. Evidence is mounting that many observed coronal loops cannot be explained by steady heating (e.g., Aschwanden, Schrijver, & Alexander 2001; Winebarger, Warren, & Mariska 2003; Patsourakos, Klimchuk, & MacNeice 2004), and that impulsive heating by nanoflares is a much more viable explanation (e.g., Cargill & Klimchuk 1997; Klimchuk 2002; Warren, Winebarger, & Mariska 2003). We plan to use the heating predicted by our MHD simulations as input to detailed loop hydro models. We will then synthesize the emission from the models and compare it with loop observations from current (*Yohkoh, SOHO, TRACE*) and future (*Solar-B,*

SDO) missions.

Finally, the properties of coronal current sheets are poorly determined at this time. As discussed in Section 6, these properties depend critically on the weak flux that surrounds kG flux tubes. The nature of this weak flux (e.g., whether and how it is fragmented and sheared in the photosphere) is itself highly uncertain. Even the parameter f that describes the partitioning of the total coronal flux between kG tubes and surrounding flux is known only approximately. This situation should change dramatically when *Solar-B* is launched and the visible-light telescope obtains images and magnetograms of unprecedented quality. We anxiously await these results and will modify our simulation parameters accordingly.

We thank G. Einaudi and M. Linton for helpful conversations. This work was supported by ONR and the NASA Sun-Earth Connection Theory and Guest Investigator Programs. Computer time was provided by the Department of Defense High Performance Computing Modernization Program.

REFERENCES

Aschwanden, M. J., Schrijver, C. J., and Alexander, D. 2001, Ap. J., 550, 1036

Bayley, B. J., Orszag, S. A., and Herbert, T. 1988, Ann. Rev. Fluid Mech., 20, 359

Berger, T. E., and Title, A. M. 1996, Ap. J., 463, 365

Bernstein, I. B., Frieman, E. A., Kruskal, M. D., and Kulsrud, R. M. 1958, Proc. Roy. Soc. (London) A, 244, 17

Biskamp, D. 1993, Nonlinear Magnetohydrodynamics (Cambridge: Cambridge Univ. Press)

Cargill, P. J., and Klimchuk, J. A. 1997, Ap. J., 478, 799

Dahlburg, R. B. 1994, Phys. Plasmas, 1, 3503

Dahlburg, R. B. 1997, J. Plasma Phys., 97, 35

Dahlburg, R. B. 1998, Phys. Plasmas, 5, 133

Dahlburg, R. B., Antiochos, S. K., and Klimchuk, J. A. 2003, Adv. Space Res., 32, 1029

Dahlburg, R. B., Antiochos, S. K., and Zang, T. A. 1992, Phys. Fluids B, 4, 3902

Dahlburg, R. B. and Einaudi G. 2001, Phys. Plasmas, 8, 2700

Dahlburg, R. B. and Einaudi G. 2002, Phys. Lett. A, 294, 43

Dahlburg, R. B. and Karpen, J. T. 1995, J. Geophys. Res., 100, 23489

Dahlburg, R. B., Montgomery, D., Zang, T. A., and Hussaini, Y. 1983, Proc. Na. Acad. Sci. USA, 80, 5789

Dahlburg, R. B., Montgomery, D. and Zang, T. A. 1986, J. Fluid Mech., 169, 71

De Moortel, I., Hood, A. W., Ireland, J., and Walsh, R. W. 2002, Solar Phys., 209, 89

Drazin, P. and Reid, W. 1981, Hydrodynamic Stability, New York: Cambridge University Press, p233

Einaudi, G., Boncinelli, P., Dahlburg, R. B., and Karpen, J. T., 1999, J. Geophys. Res., 104, 521

Forbes, T. 2002, J. Geophys. Res., 105, 23153

Furth, H., Killeen, J. and Rosenbluth, M. N. 1963, Phys. Fluids, 6, 459

Herbert, T. 1988, Ann. Rev. Fluid Mech., 20, 487

Horiuchi, R., and Sato, T. 1986, Phys. Fluids, 29, 1161

Klimchuk, J. A. 2001, in Space Weather, (Geophysical Monograph 125), ed. P. Song, H. Singer, & G. Siscoe (Washington: Am. Geophys. Un.), p. 143

Klimchuk, J. A. 2002, Inst. for Theoretical Physics Conference on Solar Magnetism and Related Astrophysics, ed. G. Fisher & D. Longcope (Santa Barbara: Univ. California) (http://online.kitp.ucsb.edu/online/solar_c02/klimchuk/)

Klimchuk, J. A., Antiochos, S. K., and Norton, D. 2000, Ap. J., 542, 504

Lin, H., and Rimmele, T. 1999, Ap. J., 514, 448

Linton, M. G., Dahlburg, R. B., Fisher, G., and Longcope, D. W. 1998, Ap. J., 507, 404

Linton, M. G., Longcope, D. W., and Fisher, G. 1996, Ap. J., 469, 954

Lionello, R., Velli, M., Einaudi, G., and Mikić, Z., 1998, Ap. J., 494, 840

Mandrini, C. H., Démoulin, P., and Klimchuk, J. A. 2000, ApJ, 530 995

Metcalfe, R., Orszag, S. A., Brachet, M. E., Menon, S. and Riley, J. J., 1987, J. Fluid Mech,, 184, 207

Meunier, N., Solanki, S. K., and Livingston, W. W. 1998, Astron. Astrophys, 331, 771

Muller, R., 1994, in Solar Surface Magnetism, ed. R. J. Rutten and C. J. Schrijver (Netherlands: Kluwer), p. 55

Nakariakov, V. M., Ofman, L., DeLuca, E., Roberts, B., and Davila, J. M. 1999, Science, 285, 862

Nakariakov, V. M., Verwichte, E., Berghmans, D., and Robbrecht, E 2000, Astron. Astrophys., 362, 1151

Ofman, L., Davila, J. M., & Steinolfson, R. S. 1994, ApJ, 421, 360

Orszag, S. A., and Patera, A. T, 1983, J. Fluid Mech,, 128, 347

Parker, E. N. 1973, J. Plasma Phys., 9, 49

Parker, E. N. 1983a, ApJ, 264, 635 bibitem[Parker(1983b)]p83b Parker, E. N. 1983b, ApJ, 264, 642 bibitem[Parker(1988)]p88 Parker, E. N. 1988, ApJ, 330, 474

Parker, E. N. 1994, Spontaneous Current Sheets in Magnetic Fields New York: Oxford University Press

Priest, E. R. 1982, Solar Magnetohydrodynamics, Dordrecht: Reidel

Priest, E., & Forbes, T. 2000, Magnetic Reconnection: MHD Theory and Applications (Cambridge: Campridge Univ. Press)

Priest, E. R,, Heyvaerts, J., and Title, A. M. 2002, ApJ, 576, 522

Schumacher, J., and Seehafer, N. 2000, Phys. Rev. E, 61, 2695

Seehafer, N., and Schumacher, J. 1998, Phys. Plasmas, 5, 2363

Solanki, S. K. 1993, Space Sci. Rev., 63, 1

Solanki, S. 2001, in Encyclopedia of Astronomy and Astrophysics, London: Nature Publishing Group, p. 2675

Stenflo, J. O., Keller, C. K., and Gandorfer, A. 1998, Ast. Astrophys., 329, 319

Warren, H. P., Winebarger, A. R., and Mariska, J. T. 2003, Ap. J., 593, 1174

Winebarger, A. R., Warren, H. P., and Mariska, J. T. 2003, Ap. J., 587, 439

Withbroe, G. L., and Noyes, R. W. 1977, ARA&A, 15, 363

This preprint was prepared with the AAS LaTeX macros v5.0.

Table 1. Simulation Parameters

Figure	ϵ_{2D}	ϵ_{3D}	$S = S_V$
2	0.002	10^{-14}	400
3	0.002	10^{-14}	400
4	0.002	10^{-14}	400
5	0.003	5×10^{-6}	400
6	0.003	5×10^{-6}	400
7	0.003	5×10^{-6}	200
8	0.002	10^{-3}	1000
9	0.002	10^{-3}	1000
10	0.002	10^{-14}	400
11	0.002	10^{-14}	400

E_d as a function of C		
C	E_d	E_d/C^2
0.1	1.18	118
0.2	3.00	75
0.3	6.15	68
0.4	11.24	70
0.5	19.02	76
0.6	30.22	84
0.7	46.21	94
0.8	171.88	269
1.0	470.90	471
1.5	2283.6	1015

Table 2.

Fig. 1.— Definition sketch of the sheared magnetic field.

Fig. 2.— Three-dimensional linear perturbed energy as a function of time parameterized by the shear parameter (C) for a case with equal fieldwise and sheetwise wavenumbers.

Fig. 3.— Three-dimensional linear perturbed energy as a function of time parameterized by the shear parameter (C) for a case with unequal fieldwise and sheetwise wavenumbers.

Fig. 4.— Dispersion relation of secondary mode with respect to sheetwise wavenumber (β).

Fig. 5.— Magnetic energy harmonic history for a low shear case ($C = 0.1$).

Fig. 6.— Magnetic energy harmonic history for a high shear case ($C = 1.0$).

Fig. 7.— Kinetic energy harmonic history for a high shear case ($C = 1.0$).

Fig. 8.— Average kinetic energy total wavenumber as a function of time for a high shear case ($C = 1.0$).

Fig. 9.— Isosurfaces of electric current magnitude, j, at four times during the 3D evolution for $C = 1.0$ and $S = S_v = 200$. The times and isosurface values are: a. $t = 177.84,\ j = 0.5814$; b. $t = 244.53,\ j = 0.4478$; c. $t = 266.76,\ j = 0.4236$; and d. $t = 288.99,\ j = 0.6017$. In panel d the data have been shifted by one half period in x and y. The structure shown in this panel is persistent at late times.

Fig. 10.— Ohmic dissipation (J/S) and viscous dissipation (Ω/S) versus time for $C = 1.0$ and $S = S_v = 1000$.

Fig. 11.— Total dissipated energy versus C for $S = S_v = 1000$. The energy has been normalized by C^2, the free magnetic energy available in the equilibrium configuration.

Fig. 12.— Perturbed energies and 5× sign δ W for $C = 1.0$.

Fig. 13.— One-dimensional to three-dimensional energy transfer terms versus time for $C = 0.3$ and 0.4.

Fig. 14.— Photospheric (left) and coronal (right) cuts across an idealized kiloGauss flux tube and surrounding weak flux. The dimension of the tube cross-section increases from d_p in the photosphere to d in the corona.

Fig. 15.— Coronal cut across an idealized array of nine circular-cross-section flux tubes.

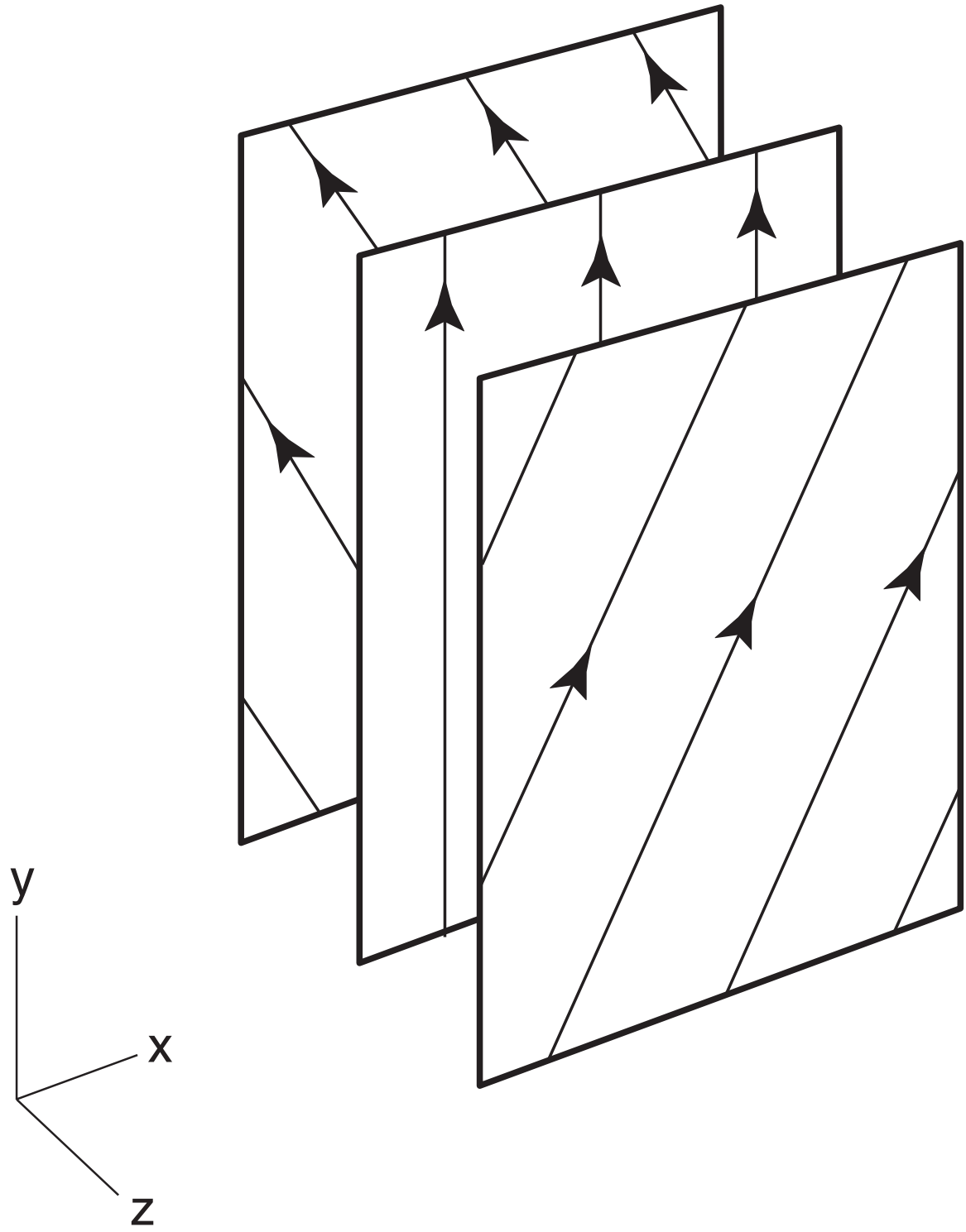

Fig. 1.— Definition sketch of the sheared magnetic field.

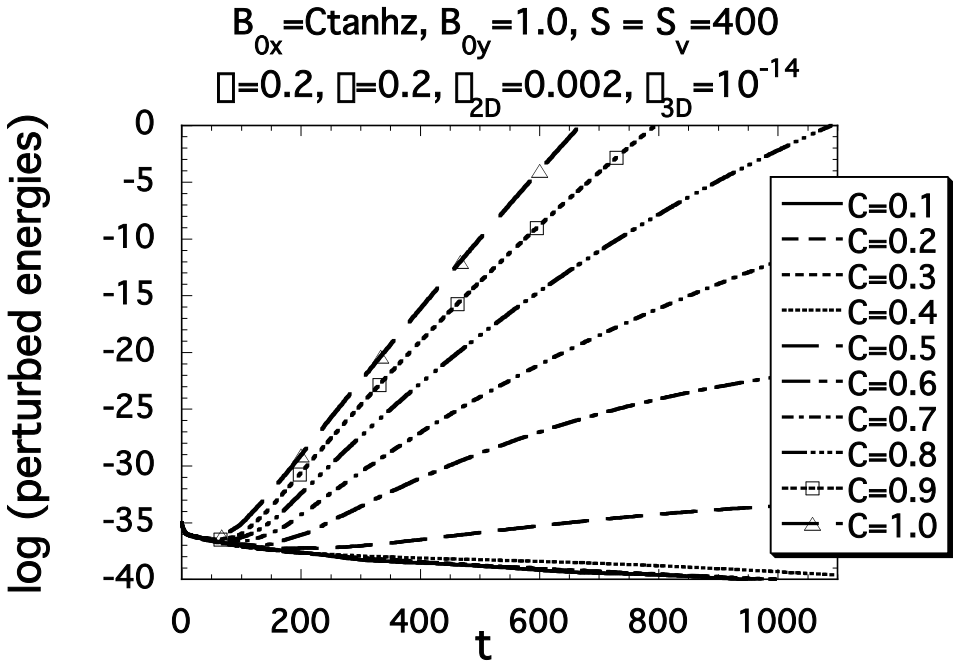

Fig. 2.— Three-dimensional linear perturbed energy as a function of time parameterized by the shear parameter (C) for a case with equal fieldwise and sheetwise wavenumbers.

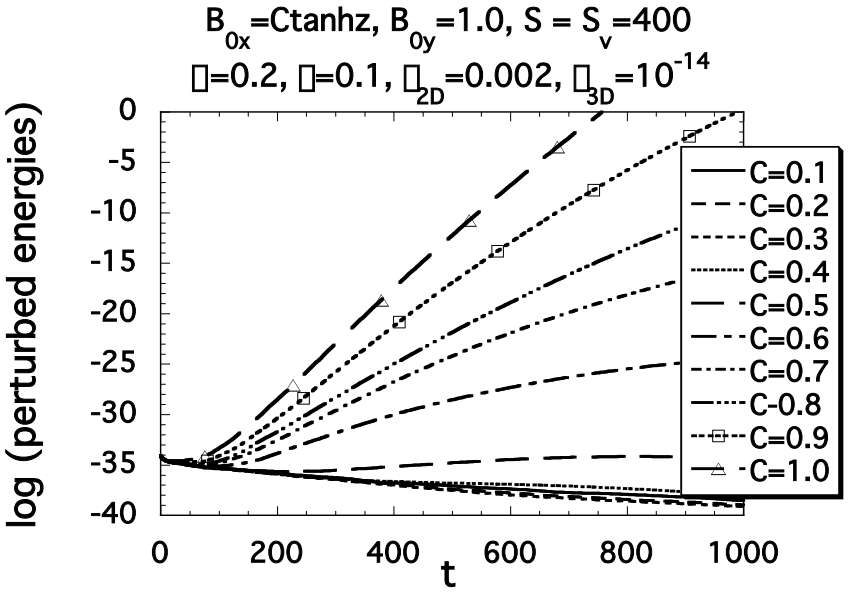

Fig. 3.— Three-dimensional linear perturbed energy as a function of time parameterized by the shear parameter (C) for a case with unequal fieldwise and sheetwise wavenumbers.

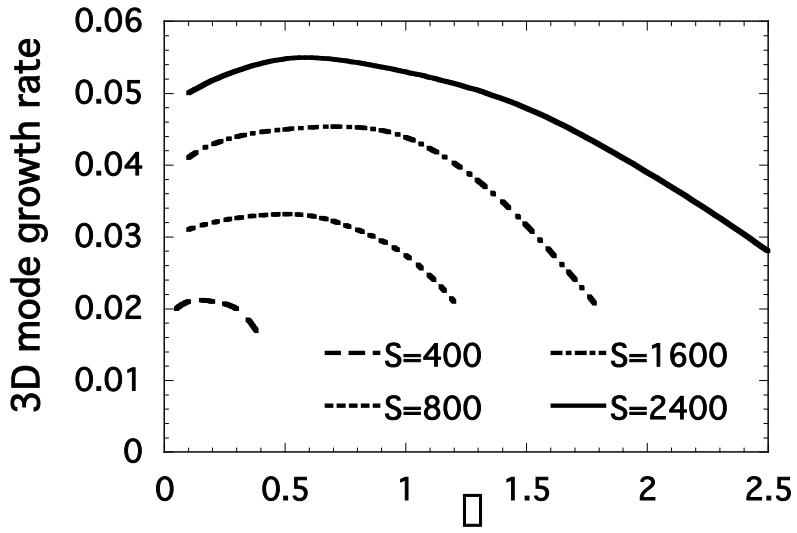

Fig. 4.— Dispersion relation of secondary mode with respect to sheetwise wavenumber (β).

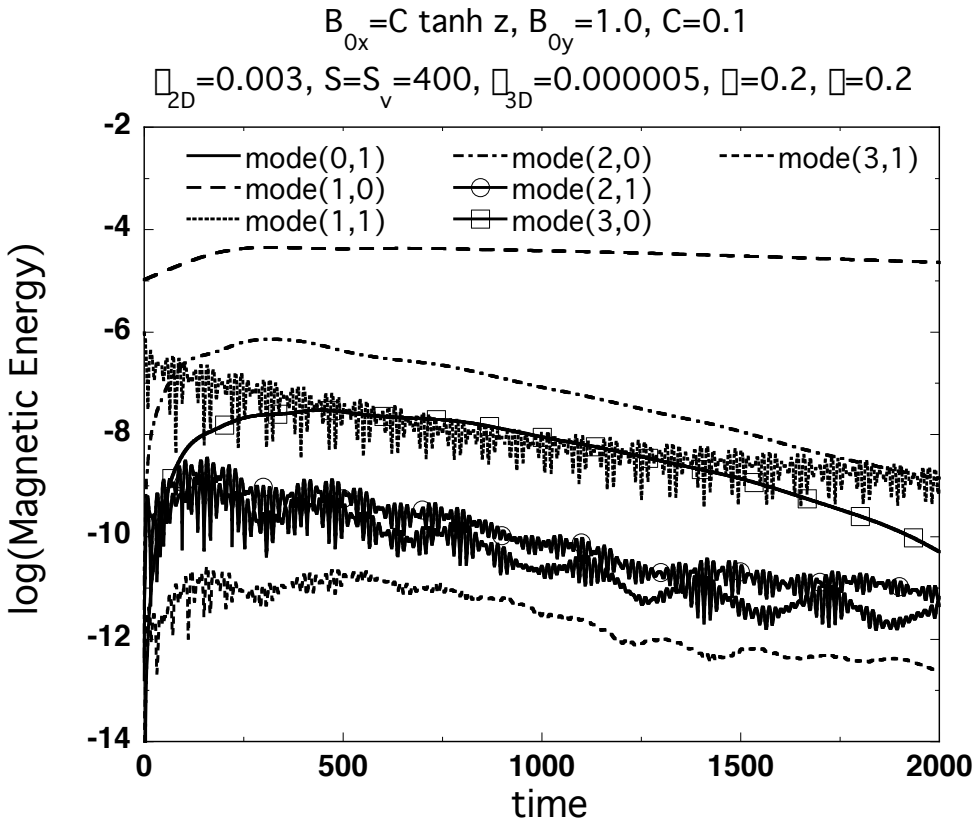

Fig. 5a.— Magnetic energy harmonic history for a low shear case ($C = 0.1$).

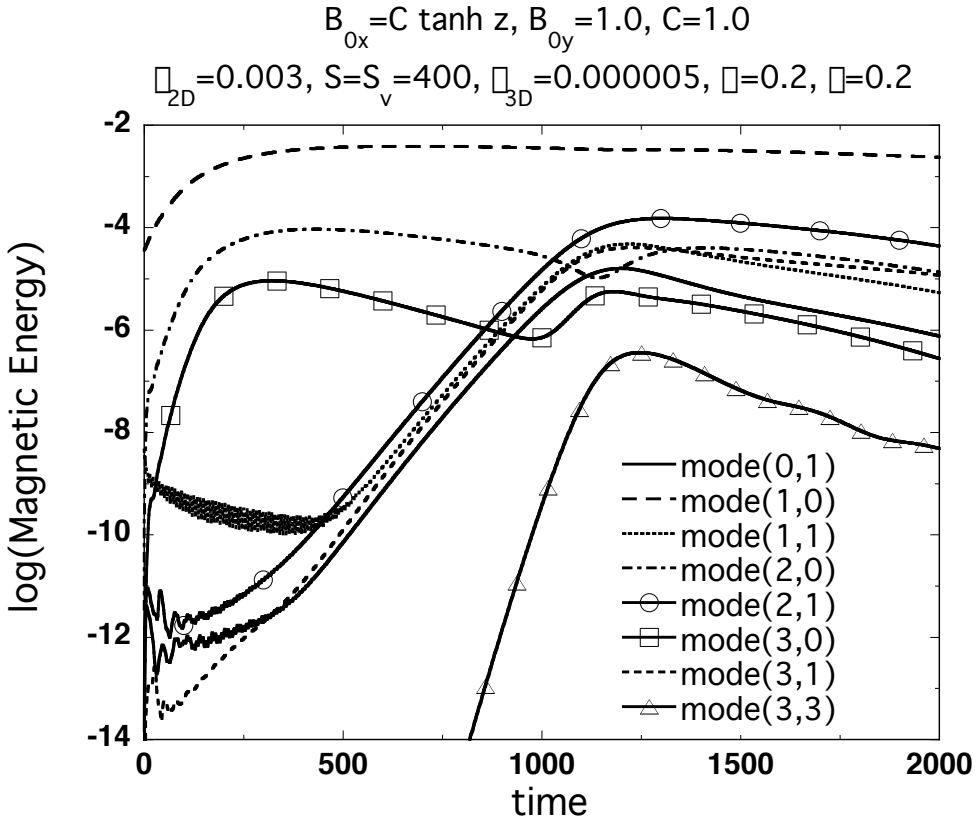

Fig. 5b.— Magnetic energy harmonic history for a high shear case ($C = 1.0$).

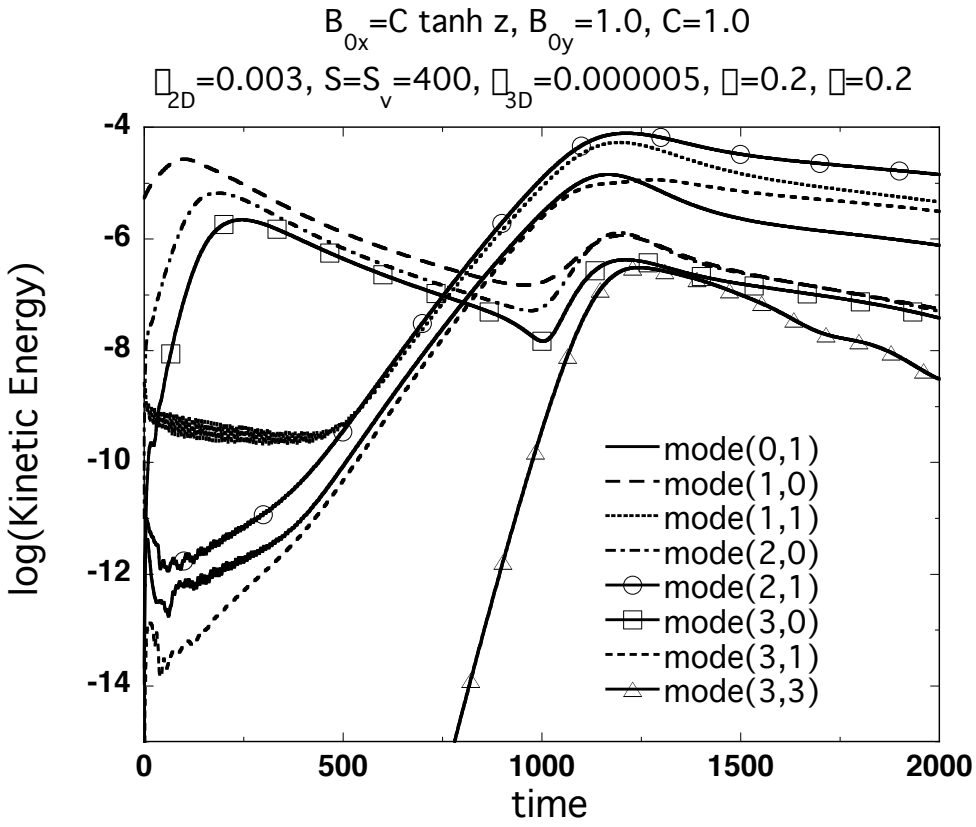

Fig. 6a.— Kinetic energy harmonic history for a high shear case ($C = 1.0$).

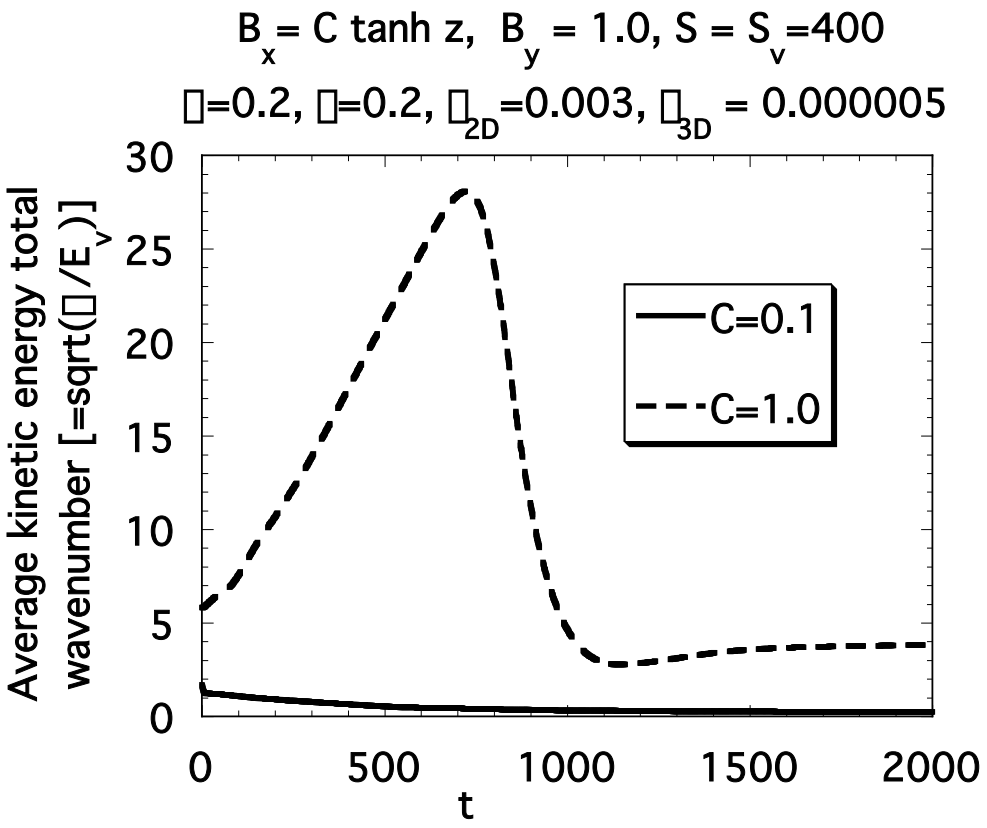

Fig. 6b.— Average kinetic energy total wavenumber as a function of time for cases of strong ($C = 1.0$) and weak ($C = 0.1$) shear.

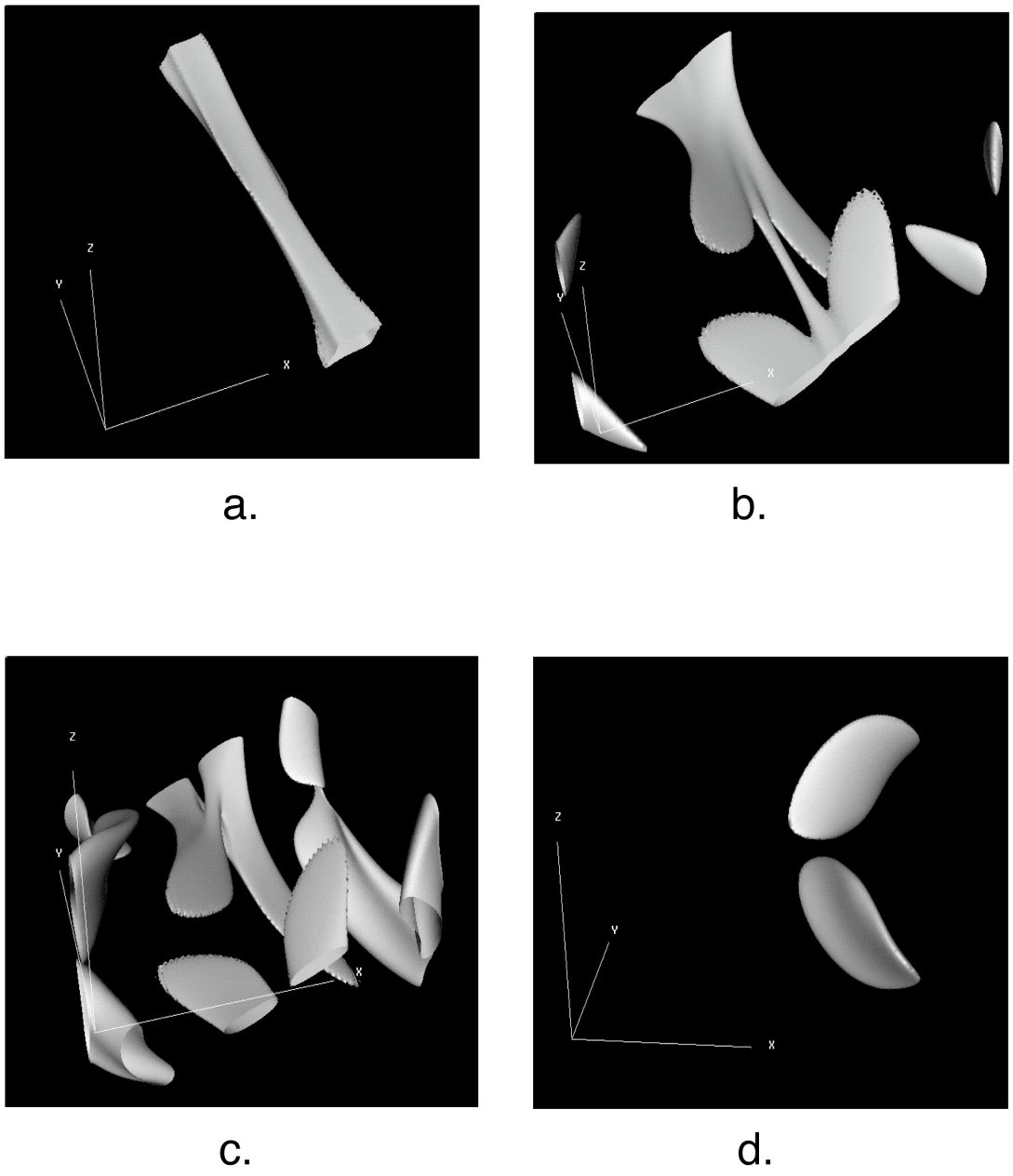

Fig. 7.— Isosurfaces of electric current magnitude, j, at four times during the 3D evolution for $C = 1.0$ and $S = S_v = 200$. The times and isosurface values are: a. $t = 177.84$, $j = 0.5814$; b. $t = 244.53$, $j = 0.4478$; c. $t = 266.76$, $j = 0.4236$; and d. $t = 288.99$, $j = 0.6017$. In panel d the data have been shifted by one half period in x and y. The structure shown in this panel is persistent at late times.

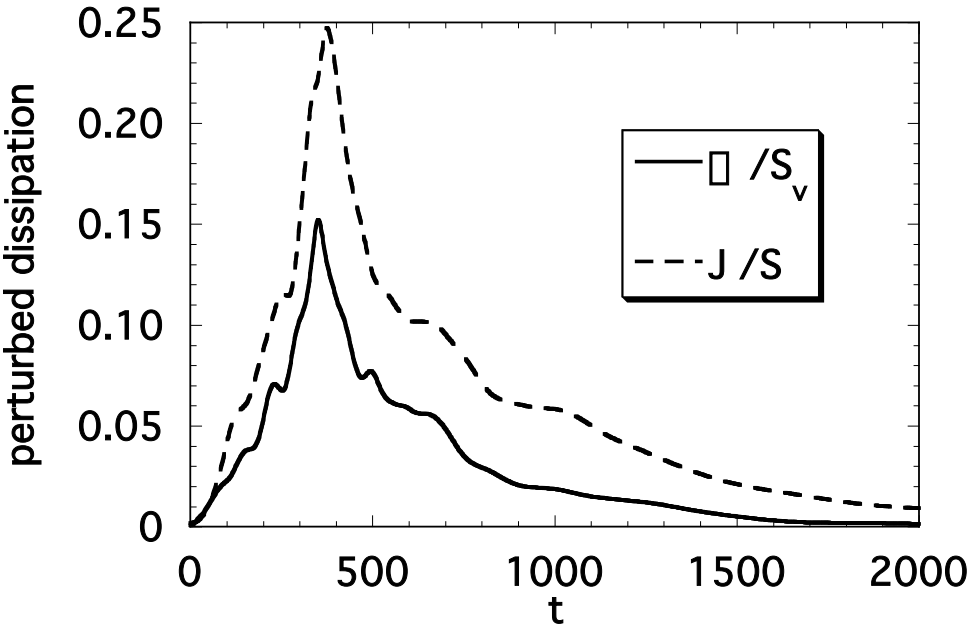

Fig. 8.— Ohmic dissipation rate (J/S) and viscous dissipation rate (Ω/S) versus time for $C = 1.0$ and $S = S_v = 1000$.

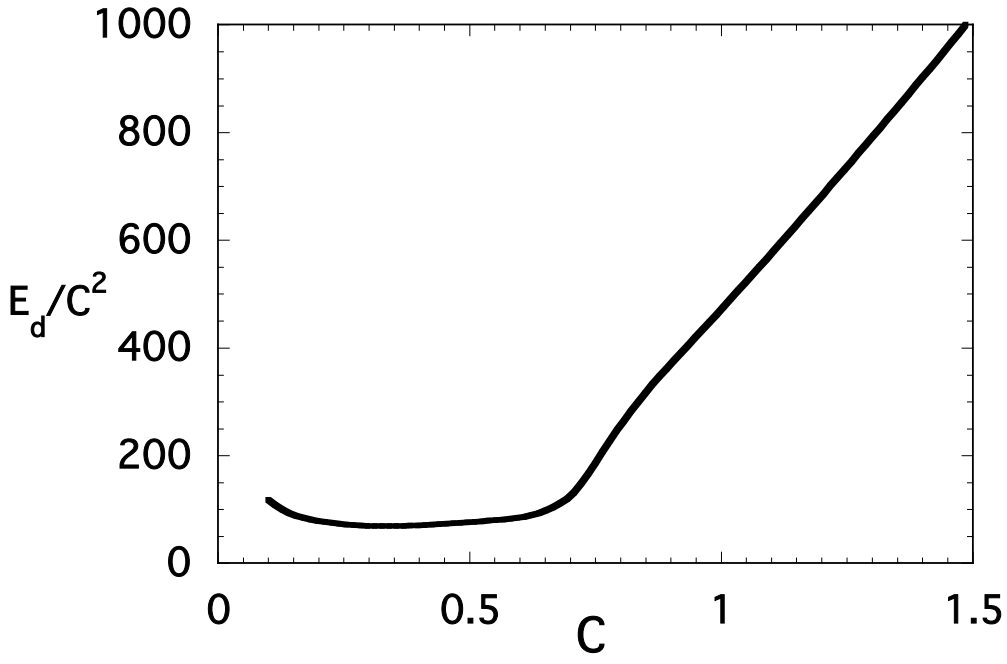

Fig. 9.— Total dissipated energy versus C for $S = S_v = 1000$. The energy has been normalized by C^2, the free magnetic energy available in the equilibrium configuration.

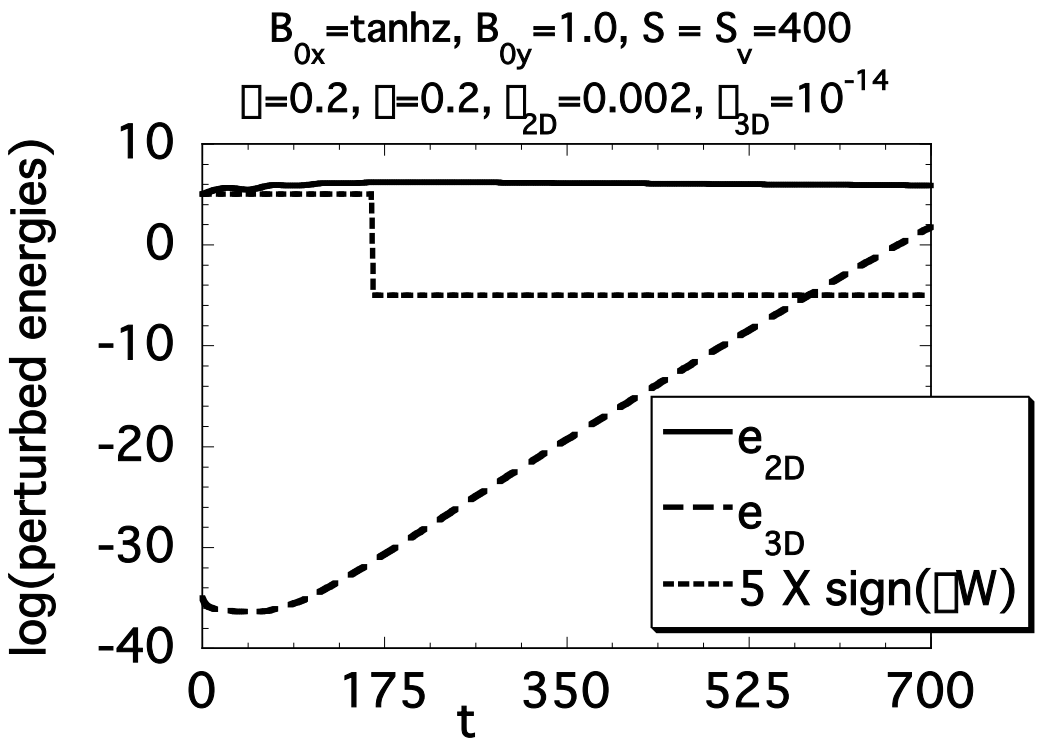

Fig. 10.— Perturbed energies and 5× sign δ W for $C = 1.0$.

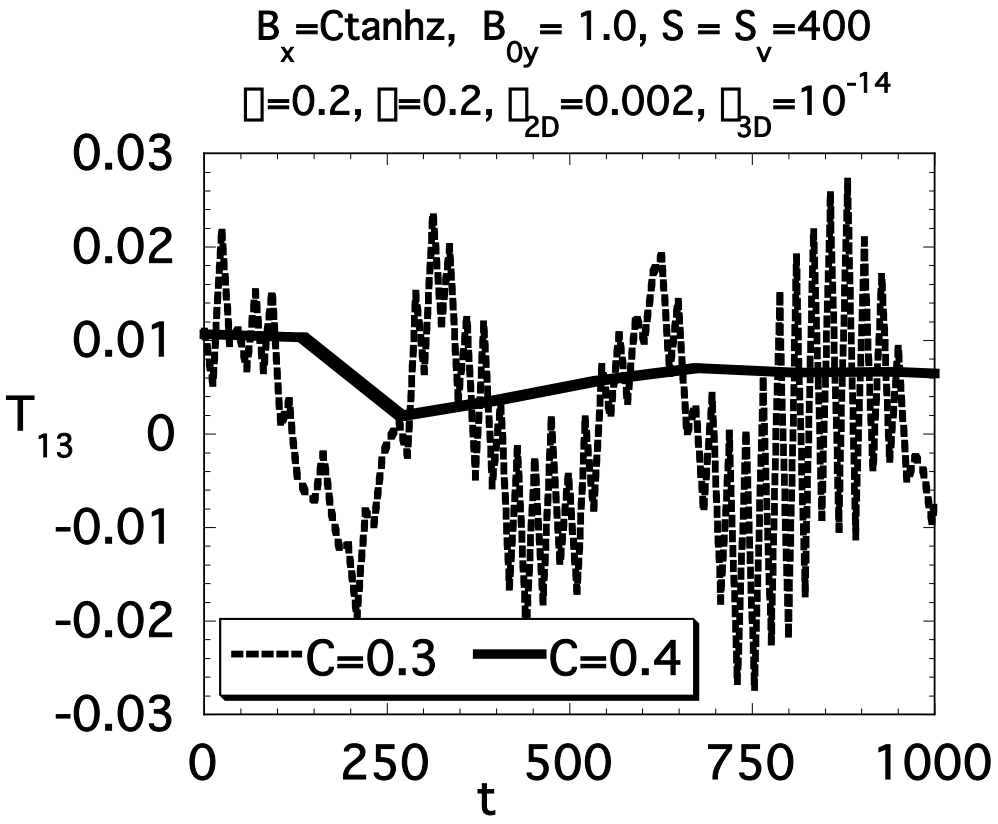

Fig. 11.— One-dimensional to three-dimensional energy transfer terms versus time for $C = 0.3$ and 0.4.

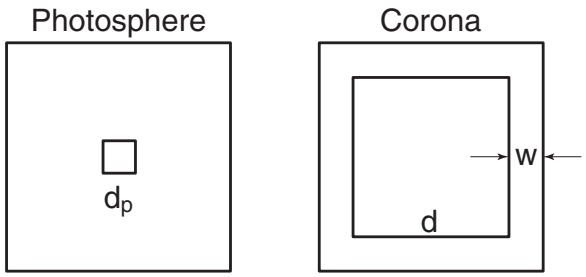

Fig. 12.— Photospheric (left) and coronal (right) cuts across an idealized kiloGauss flux tube and surrounding weak flux. The dimension of the tube cross-section increases from d_p in the photosphere to d in the corona.

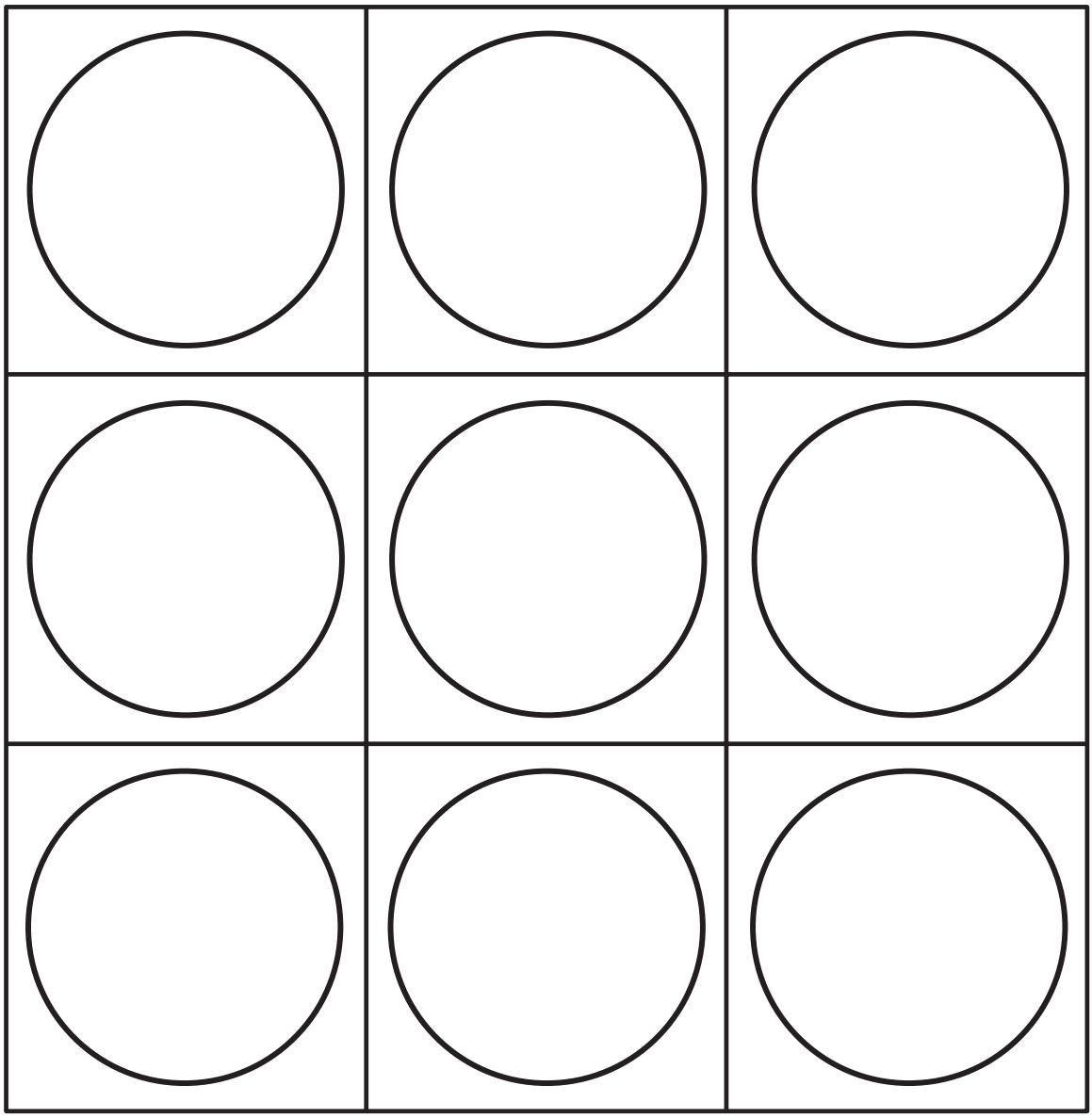

Fig. 13.— Coronal cut across an idealized array of nine circular-cross-section flux tubes.